 doi:10.20944/preprints202204.0268.v1

Article

Quantifying the Surface Strain Field Induced by Active Sources with Distributed Acoustic Sensing: Theory and Practice

Peter G. Hubbard [1]*, Joseph P. Vantassel [2], Brady R. Cox [3], James W. Rector[1], Michael Yust[2] and Kenichi Soga[1]

[1] Department of Civil and Environmental Engineering; University of California, Berkeley
[2] Department of Civil, Architectural and Environmental Engineering; University of Texas at Austin
[3] Department of Civil and Environmental Engineering; Utah State University
* Correspondence: phubbard@berkeley.edu

Abstract: Quantitative dynamic strain measurements of the ground would be useful for engineering scale problems such as monitoring for natural hazards, soil-structure interaction studies and non-invasive site investigation using full waveform inversion (FWI). Distributed Acoustic Sensing (DAS), a promising technology for these purposes, needs to be better understood in terms of its directional sensitivity, spatial position, and amplitude for application to engineering-scale problems. This study investigates whether the physical measurements made using DAS are consistent with the theoretical reception patterns and experimental measurements of ground strain made by geophones. Results show that DAS and geophone measurements are consistent in both phase and amplitude for broadband (10s of Hz), high amplitude (10s of microstrain) and complex wavefields originating from different positions around the array when: (1) the DAS channels and geophone locations are properly aligned, (2) the DAS cable provides good deformation coupling to the internal optical fiber, (3) the cable is coupled to the ground through direct burial and compaction, and (4) laser phase noise is mitigated in the DAS measurements. The theoretical relationship between DAS-measured and point-wise strain for vertical and horizontal active sources is introduced using 3D elastic finite-difference simulations. The implications of using DAS strain measurements are discussed including directionality and magnitude differences between the actual and DAS-measured strain fields. A method for spatially aligning the DAS channels with the geophone locations at tolerances less than the spatial resolution of the DAS system is proposed.

Keywords: DAS; geophones; wave propagation; strain measurement; DFOS

1. Introduction

Distributed acoustic sensing (DAS) is a technique that dynamically measures the change in length of sections of optical fiber. This is done by examining the optical path difference (OPD), or the change in distance that light travels, of Rayleigh backscatter over a length of optical fiber [1]. Rayleigh backscatter is light that propagates in the opposite direction of source laser light at the same frequency. It is caused primarily by the incident light interacting with random inhomogeneities contained within the fiber [2]. Rayleigh backscatter that has originated from different locations along an optical fiber is combined to create an interference (i.e., a superposition of wave energy). The interference pattern is used to determine the Rayleigh backscatter's phase difference between the two backscatter sources, and in-turn the evolution of the OPD between them. The average straight-line distance between the origins of the Rayleigh backscatter is called the gauge length (g). In the case of DAS, the light phase difference is the measurement output by the instrument, expressed as radians relative to the source light's average wavelength. This is converted to OPD through transformations discussed later. The phase measurements are proportional to changes in length of the fiber (due to thermal and mechanical strain), fiber refractive index, and incident light wavelength [3]. Since the measured OPD is relative to the light's wavelength, the corresponding measurements of length change (ΔL), or axial/normal

Preprints (www.preprints.org) | NOT PEER-REVIEWED | Posted: 28 April 2022 doi:10.20944/preprints202204.0268.v1

strain ($\varepsilon = \Delta L/g$) if divided by the gauge length, are extremely small. Strain measurements are examined dynamically and can be made as low as $0.6p\varepsilon/\sqrt{Hz}$ [4].

Laser phase drift and phase demodulation errors are the primary sources of noise for DAS systems. Laser phase drift is the slow variation of the wavelength of light emitted by a laser. Any deviation from the average wavelength at the source will manifest in the phase measurements. This phase noise can be reduced by high pass filtering or time-differentiating the phase data, which attenuates signals near DC (frequency = 0 Hz). The other noise source, phase demodulation errors, are the result of breakdowns of the demodulation scheme used by the DAS system resulting in incorrect phase measurements. This type of noise manifests as jumps (step functions) in the time domain phase data, or broadband noise in the frequency domain. In this study we demonstrate that: (i) the phase noise can be mitigated by high pass filtering the data within a dynamic range of interest, and (ii) phase unwrapping errors have limited impact on the recorded waveforms if the maximum sampling rate (100 kHz) of the interrogator unit is employed (Optasense Inc.'s ODH4 in the present study).

DAS has been used in the geophysical community for over a decade for measuring stress wave propagation. Specific use cases include DAS deployed in boreholes for conducting vertical seismic profiling (VSP) [5,6], within telecommunications cable conduit for ambient noise interferometry [7,8], and offshore for passive seismic monitoring [9,10]. DAS is widely accepted as a technique for detecting and measuring the phase behavior of body and surface waves. It has been described that the measurements made by DAS are approximately proportional to normal strain (ε) or strain-rate ($\dot{\varepsilon}$) [11], as defined by:

$$\dot{\varepsilon} = \frac{\left[u\left(x+\frac{g}{2},t+dt\right)-u\left(x-\frac{g}{2},t+dt\right)\right]-\left[u\left(x+\frac{g}{2},t\right)-u\left(x-\frac{g}{2},t\right)\right]}{gdt} \quad (1)$$

where u is the displacement in the direction of the cable (i.e., the x-direction), and dt is the time step between samples. It should be noted that Equation 1 assumes perfectly discrete scattering locations, when it is actually a distribution over the light pulse's shape [12]. This has allowed for the approximate conversion of DAS-measured strain to point-wise particle velocity assuming non-dispersive signals and large wavelengths relative to the gauge length of the DAS system. This relationship is:

$$\varepsilon_{xx} = \frac{du_x}{dx} = \frac{du_x}{cdt} = \frac{v_x}{c} \quad (2)$$

where c is the phase velocity of the propagating seismic wave and v_x is the particle velocity in the arbitrary x-direction. The subscript xx denotes that the strain being described is the normal strain in the x-direction from strain tensor notation.

The relationship given in Equation 2 only works as a practical transformation for DAS data when c can be easily estimated for all frequency components within the measured signal, such as isolated body wave arrivals within boreholes, as in Daley et al. [11]. For example, Wang et al. [13] applied the relationships in both Equations 1 & 2 to a surface DAS array and co-located geophones to measure long-wavelength signals at the crustal scale. It was shown that the waveforms matched well for non-dispersive signals within a frequency band of 1-5 Hz and amplitudes less than 100 $n\varepsilon/s$. This finding was significant for seismological applications of DAS, as the recorded signals were generated from a ML 4.3 earthquake and recorded across a wide aperture array of both geophones and DAS. It was noted that the amplitudes for the first few cycles were approximately the same between DAS and geophones but began to deviate later in the waveform following the S-wave arrival. This was attributed to interference between P- and S-wave coda, and a misalignment of the geophone and DAS measurement locations. In this study, we will show that DAS measurements can be consistent with geophone measurements at an engineering scale regardless of wavefield complexities for broadband and high amplitude signals.

 doi:10.20944/preprints202204.0268.v1

Most reported DAS applications have not examined the amplitude of the signals or put emphasis on converting it to physical units because the phase behavior of the measurements was of primary interest. For example, Mateeva et al. [14] presents one of the first explanations of DAS for seismic monitoring in boreholes, where a comparison between DAS and geophones is performed for picking body wave arrivals. This required identifying seismic phases in the raw data; the signal's specific amplitude or units was not used. Song et al. [15] shows the use of DAS for measuring surface wave dispersion to invert the velocity structure of the near subsurface. A step in this process is normalizing the amplitude of the traces, which is a common step in surface wave processing. Vantassel et al. [16] demonstrated that measurements of surface wave dispersion using DAS and geophone data could be compared in their respective raw units and produce essentially equivalent results, if frequency-dependent normalization was applied to the dispersion images following processing. Since the phase component of the DAS measurement alone has served the needs of the geophysical community, there has been little effort to study and quantify the signal amplitude. However, for more advanced imaging techniques, such as full-waveform inversion (FWI), both phase and amplitude are required [17]. Geophysical research has begun to move in the direction of using DAS for FWI. For example, Egorov et al. [18] used DAS VSP data for FWI. The DAS data was converted to equivalent units as the geophones using Equation 2 and then a shaping filter was applied to better match the DAS and geophone traces. This general approach has also been used by Eaid et al. [19] who also conducted FWI using shaped DAS data. Furthermore, to use DAS as an engineering tool to monitor soil structure interaction and ground deformation the amplitude of the strain measurements must be verified and not subjectively shaped.

This study aims to provide a procedure for using DAS data as quantitative ground strain measurements for stress-wave-based imaging techniques, such as FWI, that do not rely on the subjective shaping of the signal's amplitude, or for engineering problems like soil-structure interaction and ground deformation monitoring. Specifically, this study will first demonstrate how DAS data can be modeled as a finite-difference of the displacement field, and then how to practically implement a quantitative acquisition in the field. The implications of measuring a spatially differenced displacement field are explored through analytical expressions and 3D finite difference simulations of seismic waves produced by active sources. These theoretical results are compared with field-measured wavefields when an optical fiber is carefully coupled with the ground and seismic waves are created with active sources. The amplitudes of the strain measurements made with DAS are validated through quantitative comparison to geophones.

2. Analytical Representation of DAS Measurements

DAS measurements are one-dimensional. The direction of the OPD is the axial direction of the optical fiber. For the following expressions, we consider DAS measurements to be in an arbitrary x-direction as was done in Equations 1 & 2. The phase measurements made by DAS systems can be converted to relative displacement (du_x) or strain by [3]:

$$du_x = \frac{\lambda \, d\phi}{4\pi n \xi} \tag{3}$$

and

$$\varepsilon_{xx} = \frac{du_x}{g} = \frac{\lambda \, d\phi}{4\pi n g \xi} \tag{4}$$

where λ is the average optical wavelength in a vacuum of the DAS system, n is the group refractive index of the sensing fiber, ξ is the photoelastic scaling factor for longitudinal strain in an isotropic medium (= 0.78), $d\phi$ is the phase change measured by the DAS system, du_x is the relative displacement over a single gauge length of the DAS system, and ε is strain over a single gauge length.

Since velocity transducers (geophones) will be used in this study as a verification tool for DAS measurements, it is important to develop their relationship to DAS. Geophones

Preprints (www.preprints.org) | NOT PEER-REVIEWED | Posted: 28 April 2022 doi:10.20944/preprints202204.0268.v1

with a single component measure the 1D particle velocity. The spatial difference between two geophone point measurements can be used to solve for the relative particle velocity. If we align the measurement direction of the DAS and geophones and take a spatial difference over the DAS gauge length, the relative particle velocity can be expressed as:

$$dv_x = v_x(x_0 + \frac{g}{2}, t) - v_x(x_0 - \frac{g}{2}, t) \tag{5}$$

where dv is the relative particle velocity, v is the particle velocity measurement made by a geophone, and x_0 is the location exactly between two geophones spaced by g.

Note that Equation 5 is a restatement of Equation 1, except now in terms of relative particle velocity rather than strain rate. With Equation 4, the DAS measurements are then related to the geophone measurements by:

$$\frac{\delta}{\delta t} du_x = dv_x \tag{6}$$

and

$$\varepsilon_{xx} = \frac{\int dv_x \delta t}{g} \tag{7}$$

Equations 5-7 are valid only when a DAS channel is centered between two geophones with a gauge length equal to the spacing of those geophones. This is shown schematically in Figure 1. In this case the scattering centers, or the origin of the Rayleigh backscatter, is at the same location as the first order centered finite difference of the geophones. The two light pulses in Figure 1 show the position of the interrogating light pulses at the time of scattering. The two light pulses in Figure 1 may be two separate pulses, or a single forward propagating pulse whose backscatter is delayed in time [20]. The representation of a strain seismic sensor is not new and has been presented by Benioff [21] for a discrete strain sensing system. This was elaborated on by Martin et al. [22] for the case of using strain-rate DAS measurements.

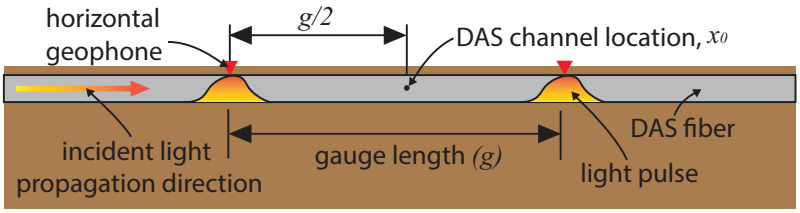

Figure 1. Schematic of DAS sensing as described by the difference between two geophones collocated with the interrogating light pulses at the time of back scattering.

Using 1D strain measurements for sensing stress waves has implications on directional sensitivity, magnitude, and phase response to different wavelengths. Martin et al. [22] presents the analytical full waveform representations of pointwise and distributed strain-rate measurements to all types of planar surface and body waves. The expressions found in that work have been time-integrated and simplified by removing the amplitude and oscillatory factors and are presented in Table 1. The purpose of these expressions is to compare the directional sensitivity of different wave types between theoretical point and DAS measurements. The directional sensitivity (d) is a multiplier of the solution to the wave equation that would determine what strain would occur as a function of the angle in the horizontal plane (θ) between an incoming wave and the 1D measurement direction of a sensor, and the wavelength of the seismic wave (λ). This is given for both a point sensor (d_ε) and a distributed measurement over a gauge length ($d_{\varepsilon,g}$). The body waves are also a function of the angle in the vertical plane (φ). Note that for a horizontally traveling body waves (i.e., φ=0) the P and Rayleigh expressions are equal, and SH and Love expressions are equal. It is important to note that these expressions assume a far-field, plane wave source which is not always a valid assumption in active source testing.

Preprints (www.preprints.org) | NOT PEER-REVIEWED | Posted: 28 April 2022 doi:10.20944/preprints202204.0268.v1

Table 1. Directional and wavelength sensitivity of point and distributed strain measurements to seismic waves (after Martin et al. [22])

Wave Type	Measurement type	Quantity	Expression
Rayleigh	point	$d_\varepsilon(\theta,\ \lambda)$	$\frac{2\pi}{\lambda}cos^2(\theta)$
	distributed	$d_{\varepsilon,g}(\theta,\lambda,\ g)$	$\frac{2}{g}cos(\theta)sin(\frac{\pi g cos(\theta)}{\lambda})$
Pressure (P)	point	$d_\varepsilon(\theta,\varphi,\lambda)$	$\frac{2\pi}{\lambda}cos^2(\theta)\ cos^2(\varphi)$
	distributed	$d_{\varepsilon,g}(\theta,\varphi,\ \lambda,\ g)$	$\frac{2}{g}cos(\theta)cos(\varphi)sin(\frac{\pi g cos(\theta)cos(\varphi)}{\lambda})$
Love	point	$d_\varepsilon(\theta,\ \lambda)$	$\frac{\pi}{\lambda}sin(2\theta)$
	distributed	$d_{\varepsilon,g}(\theta,\lambda,\ g)$	$\frac{2}{g}\sin(\theta)sin(\frac{\pi g cos(\theta)}{\lambda})$
Horizontally Polarized Shear (SH)	point	$d_\varepsilon(\theta,\varphi,\lambda)$	$\frac{\pi}{\lambda}sin(2\theta)cos(\varphi)$
	distributed	$d_{\varepsilon,g}(\theta,\varphi,\ \lambda,\ g)$	$\frac{2}{g}\sin(\theta)sin(\frac{\pi g cos(\theta)cos(\varphi)}{\lambda})$
Vertically Polarized Shear (SV)	point	$d_\varepsilon(\theta,\varphi,\lambda)$	$\frac{\pi}{\lambda}cos^2(\theta)\ sin(2\varphi)$
	distributed	$d_{\varepsilon,g}(\theta,\varphi,\ \lambda,\ g)$	$\frac{1}{g}\frac{cos(\theta)sin(2\varphi)}{cos(\varphi)}sin(\frac{\pi g cos(\theta)cos(\varphi)}{\lambda})$

If the ratio of distributed strain to point strain is calculated, it can be shown for all surface waves:

$$R_{\varepsilon,\ SW} = \frac{\lambda sin(\frac{\pi g cos(\theta)}{\lambda})}{\pi g cos(\theta)} \tag{8}$$

and for all body waves:

$$R_{\varepsilon,\ BW} = \frac{\lambda sin(\frac{\pi g cos(\theta)cos(\varphi)}{\lambda})}{\pi g cos(\theta)cos(\varphi)} \tag{9}$$

where $R_{\varepsilon,SW}$ and $R_{\varepsilon,BW}$ are the ratios of distributed to point strain for surface waves and body waves, respectively.

It is useful to visualize these expressions as a function of the ratio between signal wavelength (λ) and gauge length of a theoretical DAS system. Figure 2 shows this for the case of φ=0 along with the relative amplitude measured between DAS and a point sensor as a function of θ for P, Rayleigh, SH, and Love waves. SV waves have been omitted for brevity. For Rayleigh and P waves at λ/g=1, the DAS response is zero for incoming waves at 0°, 90°, 180°, and 270°. Love and SH waves always have zeros at 0°, 90°, 180°, and 270°, though the response of the DAS sensor is noticeably distorted from the point strain measurement at low λ/g values. As λ/g increases, the response of the theoretical DAS sensor approaches the point strain measurement. This phenomenon is important for using DAS for active source stress wave measurements because surveys need to be designed in such a way to avoid, or to expect, the zeros in the reception patterns for the waves that are being produced when either frequencies are high (i.e., short wavelengths) or when g is long. For example, an off-end survey geometry can never be expected to measure Love or direct SH waves. To avoid the zeros in the DAS reception patterns, a variety of source positions need to be used if it is desired to maximize sensitivity to all types of seismic waves, and hence maximize the information gained from a site. In the next section we develop this idea further with numerical examples of simulated DAS reception with different values of λ/g.

Preprints (www.preprints.org) | NOT PEER-REVIEWED | Posted: 28 April 2022 doi:10.20944/preprints202204.0268.v1

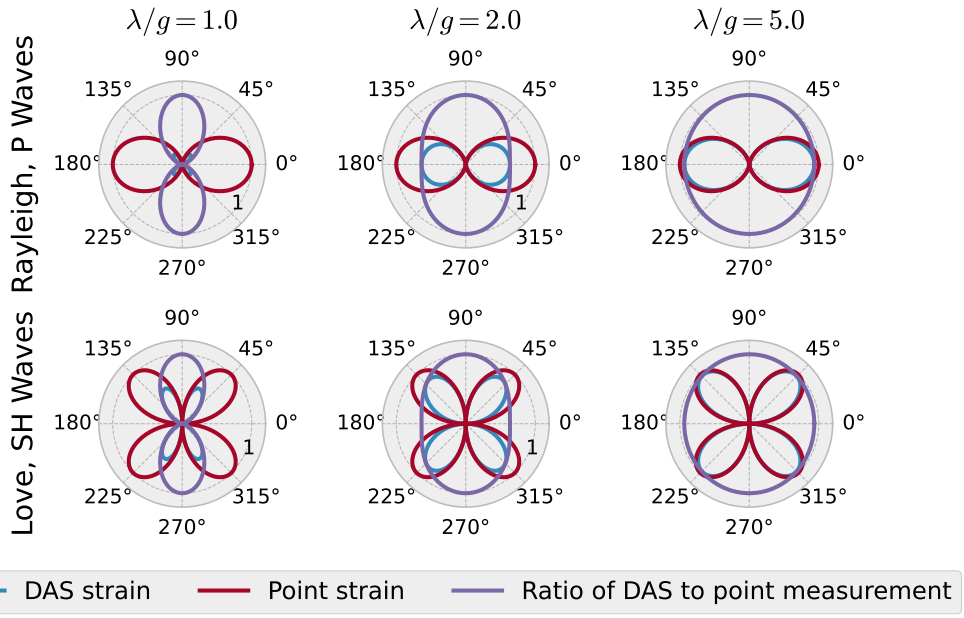

Figure 2. Radial reception patterns for point strain and theoretical DAS-measured strain for wavelength over gauge length ratios (λ/g) of 1, 2 and 5 for Rayleigh, P, Love and SH waves. In addition, the ratios of theoretical DAS strains and point strains are shown as a function of angle, which approaches unity for all wave types and angles as λ/g increases.

3. Numerical Representation of DAS Measurements

The magnitude response of DAS strain measurements is examined for their dependance on λ/g and directionality through numerically simulated DAS and point strain data. DAS data can be simulated following the relationship between point and distributed measurements described in Equations 5-7. This includes evaluating the point displacement at two locations in a model, taking a 1D difference between them in the direction of the virtual DAS cable and dividing by their separation distance.

To demonstrate this technique, 3D elastic stress wave propagation was simulated using Seismic Waves, 4th Order (SW4) node-based finite difference code [23]. The model consisted of an elastic half-space solid 200 m-wide, 200 m-long, and 100 m deep. The grid spacing was 0.5 m in all directions, resulting in 32,321,001 total grid points. The material was assigned a shear wave velocity of 250 m/s, compression wave velocity of 433 m/s and a density of 1800 kg/m^3. The velocity values created a material with a Poisson's ratio of 0.25 (also known as a Poisson solid). There was a free surface top boundary condition and absorbing super grid damping layers surrounding the model to minimize wave reflections at the boundaries. The model was excited using a point force at the top surface with a magnitude of 100 kN defined by a Ricker wavelet. The force was applied with different polarizations, including vertical, parallel to and perpendicular to the 1D strain measurement direction. This created both surface and body waves with varying wavelengths. Since the model was a Poisson solid, Rayleigh waves propagated at 0.919 times the shear wave velocity, while Love waves propagated at approximately the shear wave velocity [24].

To evaluate the numerical models in terms of λ/g, the fundamental frequency of the source wavelet was set such that the vertical source created Rayleigh waves with a 10 m wavelength (22.975 Hz), and the horizontal sources created Love waves with a 10 m wavelength (25 Hz). Displacement and pointwise strain were evaluated at each grid point at the surface of the model for each run. The displacement values across the surface were then converted to equivalent 1D DAS measurements for λ/g of 1 and 5. Essentially, each row of grid points is converted to its own 1D DAS array.

Preprints (www.preprints.org) | NOT PEER-REVIEWED | Posted: 28 April 2022 doi:10.20944/preprints202204.0268.v1

The pointwise and simulated DAS measured strain in the x-direction as evaluated 0.3 s after source initiation is shown in Figure 3 for the different source polarizations. The simulation results show the strain in the x-direction (ε_{xx}). These results can be thought of as what a DAS array oriented parallel to the x-axis will measure. The top row displays a vertical source, the center row displays a horizontal source perpendicular to the strain measurement and the bottom row shows a horizontal source parallel to the strain measurement. The three columns from left to right correspond to pointwise strain, simulated DAS strain with $\lambda/g \approx 5$ and simulated DAS strain with $\lambda/g \approx 1$, respectively. All amplitudes are normalized relative to maximum strain exhibited across all simulations.

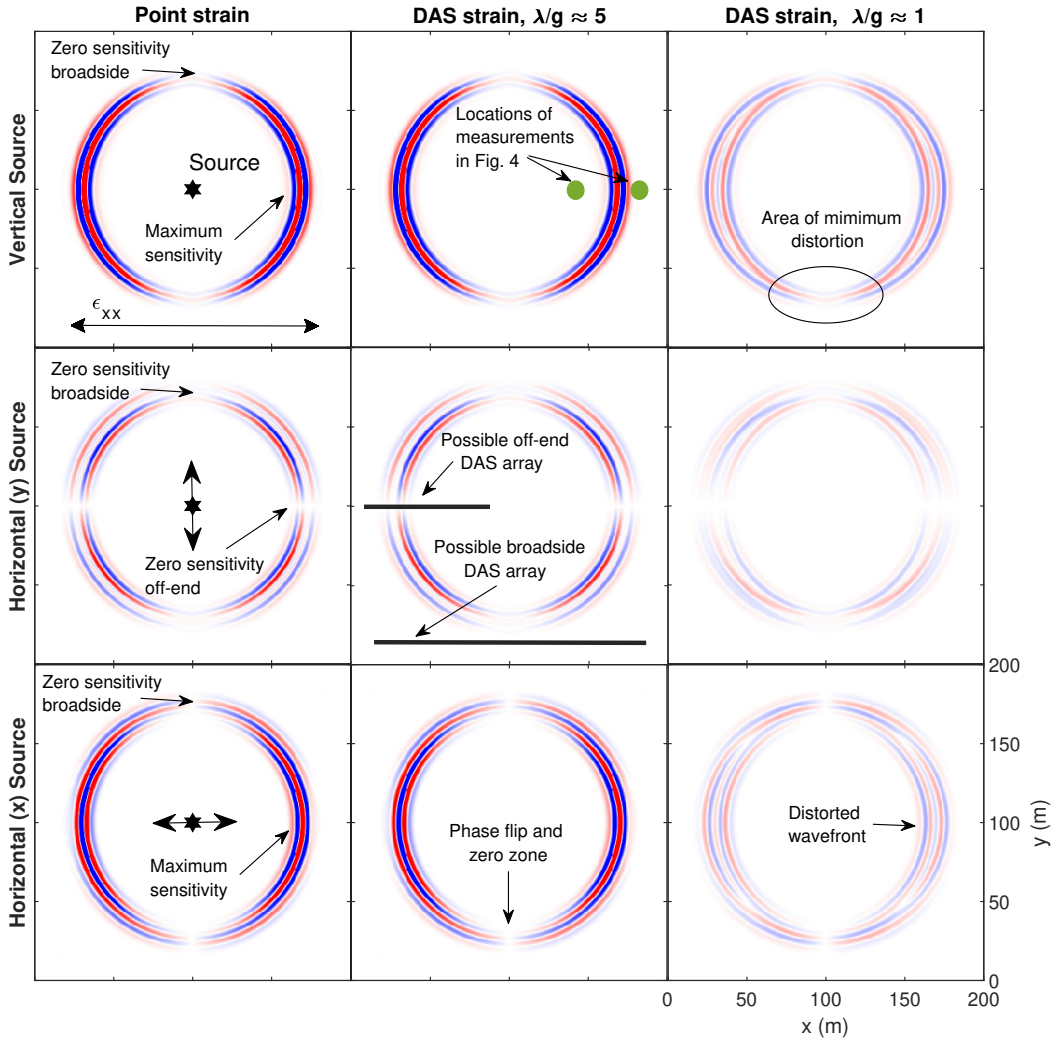

Figure 3. Simulations of normalized pointwise strain in the x-direction along the free-surface of a 200 m by 200 m by 100 m elastic half-space model caused by a 100 kN force in vertical and horizontal directions. The horizontal strain in the x-direction (ε_{xx}) is shown for each source evaluated pointwise and as measured by theoretical DAS systems aligned in the x-direction with wavelength-to-gauge length ratios (λ/g) of 5 and 1. The source is shown centered in the model to demonstrate the theoretical point strain and corresponding DAS measurements at all angles. All tiles are normalized relative to the maximum strain across all simulations. The simulations were conducted using Seismic Waves 4th Order [23].

The reception patterns for point strain and distributed DAS strain are evident in the simulation results, including zero sensitivity to perfectly broadside (90° or 270°) sources in the vertical and both horizontal directions. These zero sensitivity zones are labelled in the pointwise strain simulation results. An off-end source-receiver orientation would

Preprints (www.preprints.org) | NOT PEER-REVIEWED | Posted: 28 April 2022 doi:10.20944/preprints202204.0268.v1

result in maximum sensitivity to the vertical or x-direction horizontal source, which are also labelled, while there would be no sensitivity to the y-direction horizontal source. It is important to note the phase-flips that occur for the broadside orientation of the x-direction source and the off-end orientation for the y-direction source. This will result in strain with an opposite sign being measured depending on what side of this phase-flip the receiver is on. This will be evident later in the field-acquired data.

The wavefields are captured well by the simulated DAS data for the case of $\lambda/g \approx 5$. The wavefronts have a significantly lower amplitude and become distorted when $\lambda/g \approx 1$. This is most evident for the y-direction horizontal source. Importantly, the distortion diminishes toward the broadside source-receiver orientation, which is labelled in the top-right tile. This observation is consistent with Equations 8 and 9, and Figure 2 that demonstrate that the ratio of DAS strain to point strain approaches one for angles near 90° and 270° degrees regardless of λ/g.

The amplitude distortion caused by low λ/g values is shown in Figure 4. The off-end source-receiver orientation for a vertical source is shown for measurement offsets of 40 and 80 m relative to the source. The location of these receivers is also indicated in the top-center tile of Figure 3. The $\lambda/g \approx 5$ case is very close of the point strain amplitude. The measured amplitude diminishes for the $\lambda/g \approx 2.5$ case before becoming completely distorted for $\lambda/g \approx 1$. For a monochromatic plane wave solution, the $\lambda/g \approx 1$ case would result in zero strain measured (see [16]); the strain is non-zero because the source Ricker wavelet has a non-finite bandwidth. This result is important because it indicates how DAS arrays will fundamentally respond to the most common active source and geometry, the off-end hammer strike. Due to the wide bandwidth of the wavelet generated by an impulse signal like a hammer or weight drop, the ability for DAS to adequately measure the pointwise strain field is a function of λ/g. This can be mitigated if either the user quantifies the amplitude reduction due to the λ/g ratio for the particular application or, preferably, examines the spatially differenced displacement field as the desired quantity in their forward modelling of a problem.

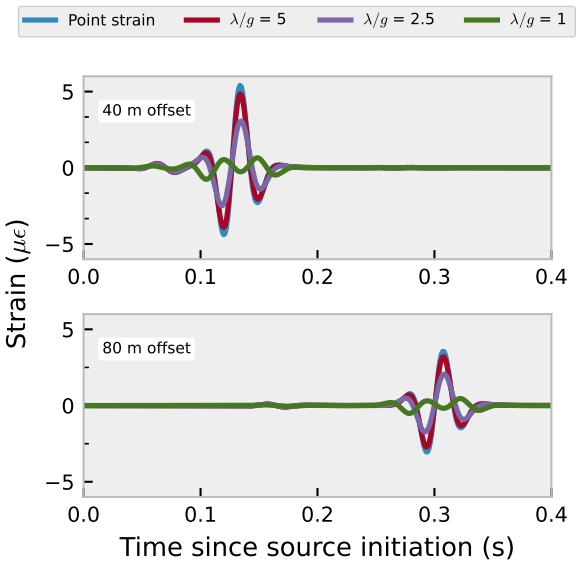

Figure 4. Simulations of DAS measured strain along the free surface of an elastic model at offsets of 40 and 80 m caused by a 100 kN force in vertical direction. Wavelength-to-gauge length ratios of 1, 2.5 and 5 relative to the Rayleigh wavelength are shown for a virtual DAS array extending radially away from the source position. The simulations were conducted using Seismic Waves 4th Order [23].

Preprints (www.preprints.org) | NOT PEER-REVIEWED | Posted: 28 April 2022 doi:10.20944/preprints202204.0268.v1

4. Experimental Campaign

An experiment was conducted at the NHERI@UTexas [25] Hornsby Bend test site in Austin, TX to compare active source seismic strain signals recorded simultaneously using DAS and geophones. An aerial photograph of the test setup is shown in Figure 5. The test used a 94 m-long geophone array (48 geophones at 2 m spacing) directly above two different 200 m-long fiber optic cables buried in a shallow trench. The cables were installed carefully to ensure good coupling with the ground.

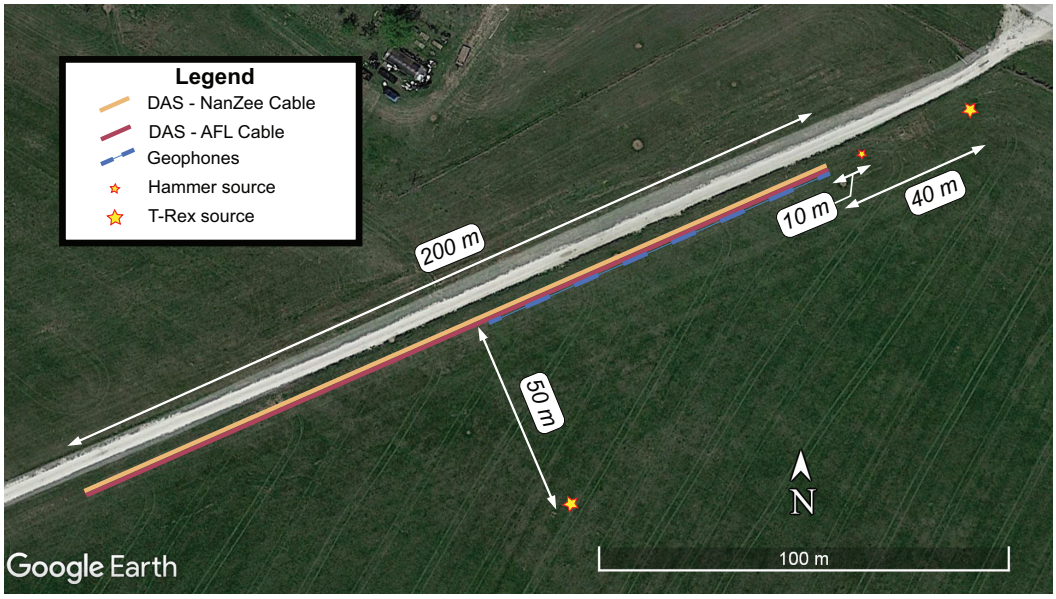

Figure 5. Plan view of the experimental setup at the Hornsby Bend test site along Platt Lane in Austin, TX, USA, where a 94 m geophone array and two 200 m DAS arrays (NanZee and AFL cables) were installed at the same location. The geophones were spaced at 2 m and the gauge length of the DAS system was 2.04 m. The two different DAS cables were spliced together at the far end of the array and interrogated simultaneously. The T-Rex vibroseis truck was used to vibrate the ground 40 m from the arrays in an off-end configuration and 50 m from the arrays in a broadside configuration. A sledgehammer was used to strike the ground vertically 10 m from the arrays in an off-end configuration.

The cable installation process is shown in Figure 6a-c. First, the end points of the trench were surveyed with a total station and a line was pulled tight to mark the position of the trench. Next, a trenching machine was used to excavate a 10-15 cm deep trench along the marking line (Figure 6a). Once the trench was excavated, the cables were placed side-by-side at the bottom of the trench (Figure 6b). The trench was then backfilled using the same volume of soil that was removed. A skid-steer loader was used to push the soil into the trench and then driven on top to compact the soil (Figure 6c).

The fiber optic cable selection is of particular importance for quantitative deformation measurements. Two cables with tightly buffered optical fibers were used. One was NanZee Sensing Technology's NZS-DSS-C02 (Figure 6d), and the other was AFL's X3004955180H-RD (Figure 6e). Note that tight buffering only refers to the layer directly outside the optical fiber [26], such that a polymer coating was applied directly to each individual fiber. Outside of that tight buffer the construction can vary widely from one cable design to another. The NanZee cable has a layer of steel braid that is wound securely around a single tight buffered fiber, which is then encased in a polyethylene jacket. The AFL cable, in contrast, has a layer of aramid yarn surrounding four tight buffered fibers encased in a polyurethane jacket. It can be assumed from the construction that the AFL cable will be much less-stiff than the NanZee cable, though the actual stiffness values were not tested.

The cables were fusion spliced together inside a junction box so that they could be simultaneously interrogated using a single DAS interrogator unit (IU), which for this study

Preprints (www.preprints.org) | NOT PEER-REVIEWED | Posted: 28 April 2022 doi:10.20944/preprints202204.0268.v1

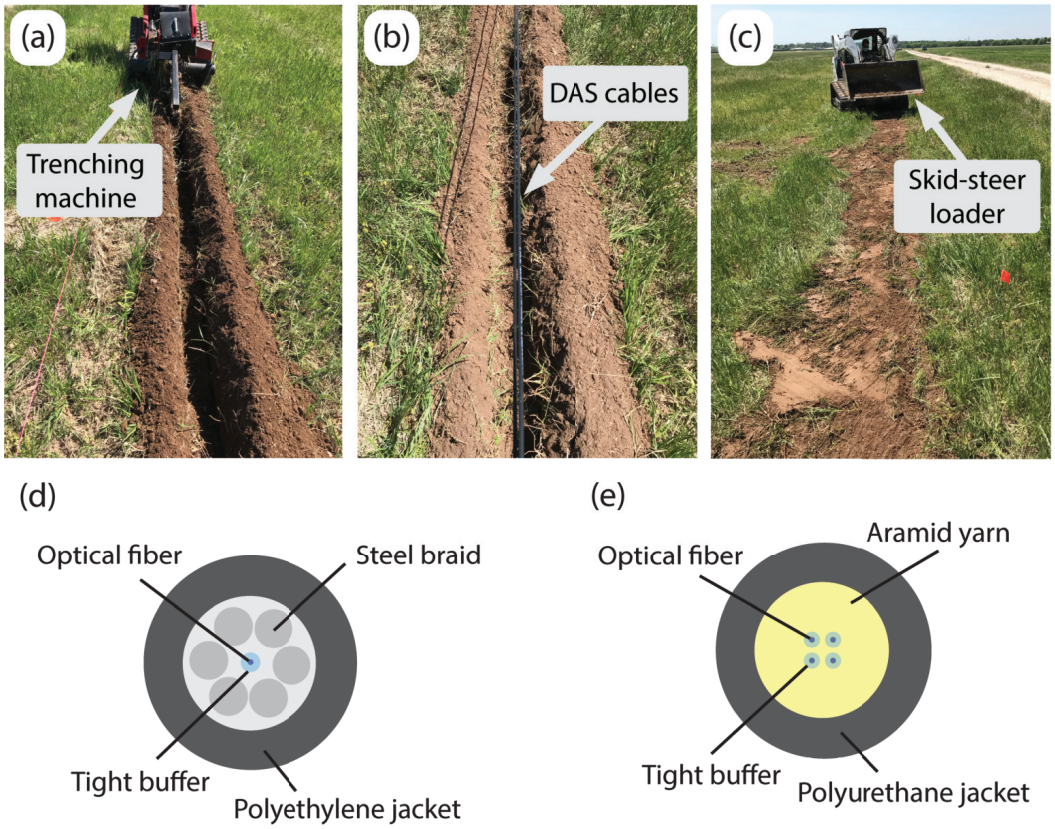

Figure 6. The fiber optic cables were tightly coupled with the ground by: (a) using a trenching machine to excavate a trench between 10 and 15cm deep, (b) placing the two cables within the trench next to each other, and (c) backfilling and compacting the trench with a skid-steer loader to ensure the soil was densified around the cables. The two installed cables were (d) NanZee Sensing Technology's NZS-DSS-C02 and (e) AFL's X3004955180H-RD.

was an OptaSense ODH4. One end of the cables was brought into an instrumentation trailer that housed the IU, geophone data acquisition systems, and vibroseis control electronics. The other end was terminated to reduce end-reflections during DAS data acquisitions. The OptaSense ODH4 IU was configured to have a gauge length of 2.04 m, a channel spacing of 1.02 m, and a pulse repetition rate of 100 kHz. Due to the demodulation scheme used by the ODH4, which determines the optical phase over four consecutive pulse repetitions, the 100 kHz pulse rate produces a sensing bandwidth of 12.5 kHz. The DAS data was decimated in real-time to 1 kHz. The horizontal geophones used were Geospace Technologies GS-11D with a fundamental frequency of 4.5 Hz. The geophones were housed in PC21 land cases with 7.6 cm aluminum spikes. They were oriented horizontally along the direction of the DAS cables (i.e., in-line) for direct comparison to the DAS data. There were 48 geophones spaced at 2 m for a total array length of 94 m. The geophones were connected to two 24-channel Geometrics Geode seismographs. Geophone measurements were also collected at 1 kHz.

One week after cable installation, seismic waves for the study were generated by two different sources: (1) the NHERI@UTexas vibroseis truck T-Rex, and (2) a sledgehammer. Wavefields generated by the seismic sources were recorded simultaneously using both the DAS and geophone arrays. T-Rex is a three-dimensional vibroseis truck that can shake its baseplate vertically, in-line, and crossline [25]. T-Rex has a maximum output force of approximately 267 kN and 134 kN in the vertical and horizontal directions, respectively. The source signal generated by T-Rex was a linear chirp from 3 to 80 Hz over 12 s. As shown in Figure 5, this paper presents measurements made when T-Rex was: (i) 40 m from the beginning of the DAS and geophone arrays in an off-end configuration, as well as (ii)

 doi:10.20944/preprints202204.0268.v1

50 m broadside from the arrays. A sledgehammer striking the ground vertically at 10 m from the array in an off-end orientation is also presented.

5. Experimental Evaluation of DAS Reception Patterns

First, the DAS-recorded measurements using the NanZee cable are presented qualitatively to examine the impacts of DAS reception on signal characteristics. As discussed later, both cables were of sufficiently high quality and good coupling such that the cable choice made little difference in signal measurement. Figure 7 shows seismic recordings of DAS data cross-correlated with the T-Rex source sweep signal. This cross-correlation results in a zero-phase source wavelet with center frequency of 41.5 Hz. The data is shown for both off-end and broadside configurations of the vertical and both horizontal directions of excitation using the T-Rex vibrosies source. The DAS array is oriented in the x-direction. The data is shown normalized relative to the maximum amplitude across all the records for straightforward comparison.

The off-end configurations (the left tiles in Figure 7) give maximum signal amplitude for the vertical source and horizontal source oscillating in-line with the x-direction. As expected from the simulations presented in Figure 3, the y-direction horizontal source (i.e., cross-line shaking) produces a much smaller signal received on the DAS array. For the broadside source position (the right plots in Figure 7), the reception patterns of DAS are more obvious. All three source directions cause a minimum signal reception where the angle of incidence is 270°. However, as shown from the simulations presented earlier, only the horizontal source excited in-line with the x-direction sees a phase-flip at the 100 m location. These results provide experimental evidence supporting the reception patterns postulated by Benioff and Martin et al. [21,22] and further described by the numerical simulations presented in this work. The actual strain signal amplitudes are verified in the next section.

Preprints (www.preprints.org) | NOT PEER-REVIEWED | Posted: 28 April 2022 doi:10.20944/preprints202204.0268.v1

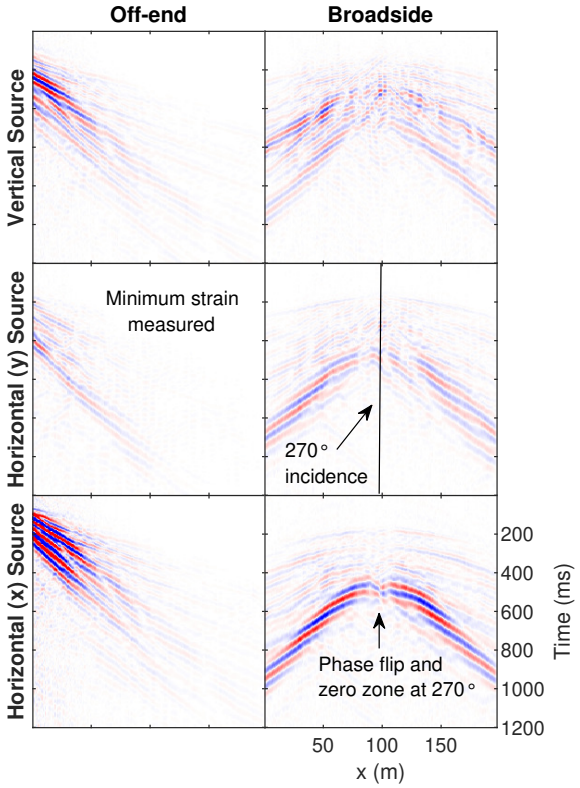

Figure 7. Experimental results of testing the angular reception pattern of DAS subject to active source vibration in both off-end and broadside configuration for vertical and both horizontal directions of excitation using the T-Rex vibrosies source. The DAS array is oriented in the *x*-direction. The off-end geometry is 50 m from the beginning (x=0) of the DAS array, and the broadside configuration is 50 m perpendicular from the midpoint of the200-m-long DAS array.

6. Comparison of Strain Measurements from DAS and Geophones

In this section, geophones are used to verify the amplitude of the strain measurements made with DAS. The first processing step of processing the DAS data is to mitigate the phase noise at low frequencies. To do so, a 3 Hz high pass filter was applied to the raw DAS phase measurements and then the measurements were converted to strain using Equations 3 and 4. The geophone measurements were converted from the raw form to particle velocity by compensating for their frequency dependent response and gain of the seismographs. Next, the velocity time-series were integrated in the frequency domain to achieve units of displacement. The displacement measurements from each geophone were subtracted from the next geophone in the array to create a spatial difference, and the result was divided by the geophone spacing to get unitless strain. This is exactly like the process for simulating the DAS data in the numerical example presented previously. Then, a DAS channel at about the same location as the differenced geophones was selected for comparison.

6.1. Uncertainty in DAS Channel Location

The result when T-Rex vibrated the ground at a location of 40 m from the array is shown for six different DAS channels and differenced geophone pairs in Figure 8. For a clear view of the waveforms, 0.25 s of data are shown from 1.50 – 1.75 s into the 12 s long, 3-80 Hz vibroseis chirp. The amplitudes of both DAS cable measurements match well to the amplitudes of the spatially differenced geophone measurements.

Preprints (www.preprints.org) | NOT PEER-REVIEWED | Posted: 28 April 2022 doi:10.20944/preprints202204.0268.v1

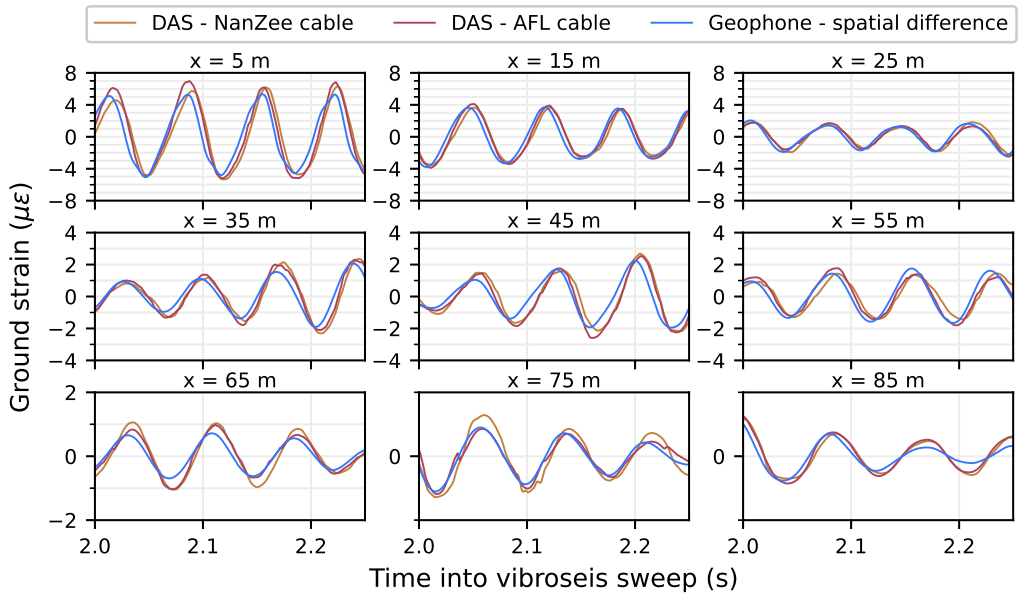

Figure 8. Temporal comparison of spatially averaged particle velocities measured with DAS on both the NanZee and AFL cables with spatially differenced geophone measurements during in-line shaking by T-Rex 40 m from the array performing a 12-second, 3-80 Hz chirp. Each geophone used for differencing was close to the locations of the scattered optical pulses, but not perfect (see Figure 9). The position indicated is the point between the two differenced geophones (i.e. 75 m indicates the data from subtracting the geophone at 74 m from the one at 76 m). The geophone data has been corrected for instrument response and converted to units of displacement through integration. The spatially differenced geophone measurements were then divided by the geophone spacing to produce a value of strain.

There is a slight phase difference (i.e., time shift) between the time series for all locations, as shown in Figure 8. This is consistent with the phenomena observed by Wang et al. [13] and Egorov et al. [18]. This phase difference is due to the uncertainty associated with the DAS measurement location relative to the geophone positions. As shown in Figure 9, when a DAS system is operated, the sensing fiber is interrogated at a fixed spatiotemporal frequency determined by the digitizer of the DAS system. The measurement channels are evenly spaced but the exact position is hard to determine. Often a 'tap-test' is performed by tapping at a known location and examining what DAS channels respond. However, this is only able to locate the measurement point with a certainty of the gauge length of the DAS system (i.e., +/- one half of a gauge length). Therefore, it is expected that there will be a slight shift in the measurement location between colinear DAS and geophone arrays even when a tap-test is performed. The method that is developed here for aligning the DAS and geophone data does not require a tap-test, though it is assumed the relative position between DAS and geophones is first correctly estimated within 10 m.

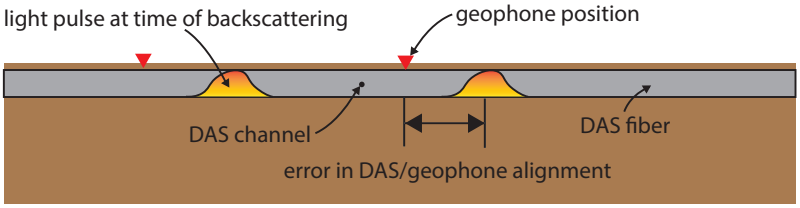

Figure 9. Schematic of the spatial uncertainty of the location of DAS channels in relation to a geophone on the ground surface for a linear DAS array. It is not possible to perfectly locate the scattering positions in DAS arrays so there will be error between DAS and geophone positioning.

6.2. Correcting spatial offset between Geophones and DAS

A method for aligning DAS channels with spatially differenced geophone measurements is proposed here. The method includes spatially up-sampling the DAS data using Fourier method interpolation [27] so that synthetic DAS channels exist every 1 cm along the array. Then, the spatially up-sampled DAS channels are compared to the geophone measurements. This is done by comparing each 1 cm-spaced synthetic DAS channel in the vicinity of a geophone pair with the spatially differenced time-series from that pair. The time series from both DAS and geophones are normalized by their two-norm and then the sum of the square error at each time sample is taken as the misfit. The minimized value achieves relative alignment between the scattering locations used for DAS and the geophones. The misfit is described by:

$$m_x = \Sigma_{i=1}^{n} \left(\frac{D_{i,x}}{\|D_x\|_2} - \frac{G_i}{\|G\|_2} \right) \tag{10}$$

where D_x is the time-series of DAS data at location x of length n points, G is the time-series defined by a spatially differenced geophone pair, and m_x is the misfit calculated for that DAS time-series and geophone pair location.

Figure 10a shows an example of how this procedure works using the NanZee cable data from the vertical T-Rex shake 40 m from the array. The magenta traces are the first 20 DAS traces spaced at 1.02 m which is the default trace separation of the ODH4 IU. The grey variable density image behind the traces is the interpolated wavefield sampled every 1 cm in space. The red traces are shifted to minimize the misfit described by Equation 10 between the DAS and geophone measurements while being constantly spaced at 1.00 m. This process simultaneously corrects for the mismatch in the geophone/DAS channel positions and spacing. Figures 10b and 10c show the minimization result relative to the position of the first DAS trace in the array for 40 DAS traces and geophone pairs. The results show that the estimated locations of the NanZee cable's first DAS trace was offset from the geophone positions by about 77 cm, while the AFL cable's array was offset by about 30 cm. The corresponding new 1.00 m spaced, interpolated DAS channels can be selected to create a shifted DAS array that resolves the phase mismatch with the geophones observed previously (recall Figure 8). It is important to note that the spatial interpolation can only be considered valid for wavelengths larger then twice the trace separation, 2.04 m in this case, based on the Nyquist-Shannon sampling theorem.

Preprints (www.preprints.org) | NOT PEER-REVIEWED | Posted: 28 April 2022 doi:10.20944/preprints202204.0268.v1

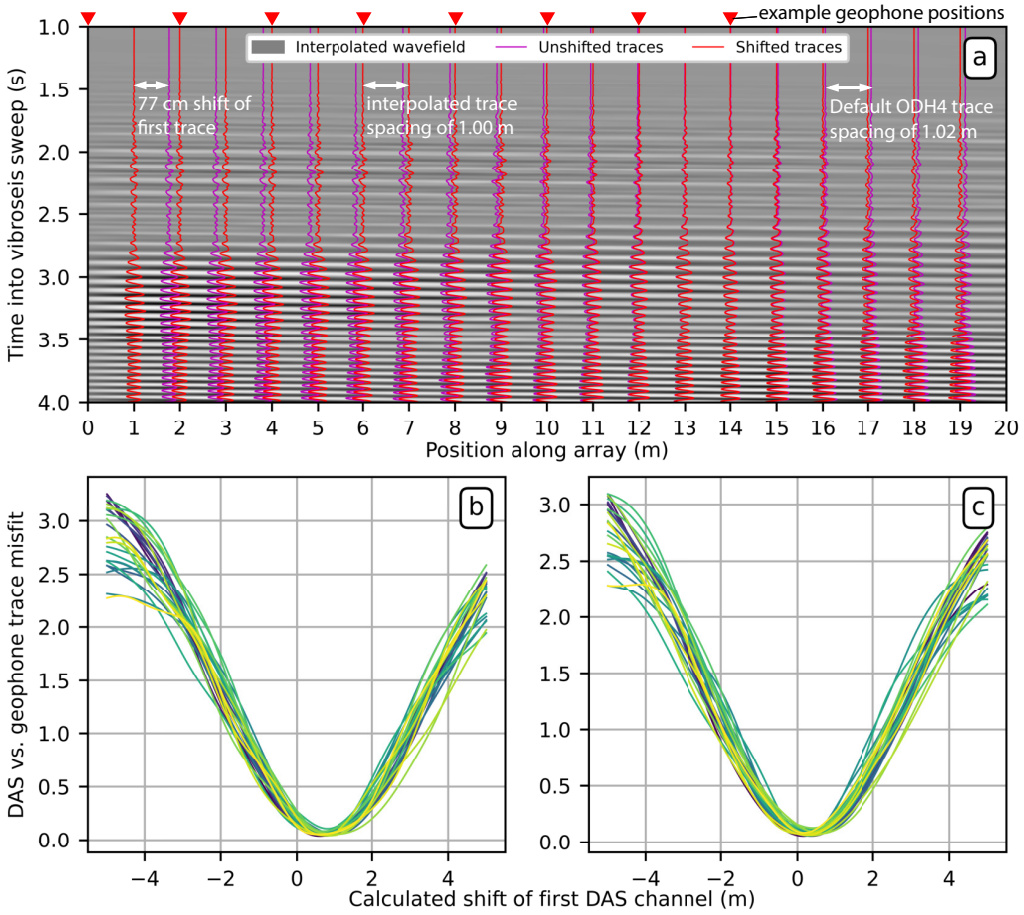

Figure 10. (a) Demonstration of the proposed method to align DAS arrays in space with geophones using the NanZee cable array and data from the vertical T-Rex shake 40 m from the array. The measured wavefield (magenta traces) is upsampled in space using Fourier interpolation to 1 cm trace separation and shown as the grey variable density background. Each 1 cm-spaced trace is compared to geophone-calculated strain data where the position of the discrete geophones is known. The new 1.00 m spaced set of DAS traces that minimize the misfit between the DAS and geophone measurements are selected (red traces) creating a DAS array where the position of each trace is known. (b) and (c) show the minimization result for the relative position of 40 DAS traces relative to geophone pairs for the NanZee and AFL cables, respectively. The green colors are different DAS trace/geophone measurement comparisons shown relative to the shift of the first DAS trace in the arrays. It is necessary to make comparisons relative to the shift of the first trace because the arrays have different spacing (1.02 m vs. 1.00 m), which is ultimately resolved in the interpolation process.

6.3. Vibroseis Truck Shaking

Measurements from the 77 cm shifted NanZee cable and 30 cm shifted AFL cable DAS arrays are compared with the spatially differenced geophones in Figures 11 for a T-Rex vibroseis chirp. The figure shows 0.5-6 s from the time the vibration was triggered at various locations along the array. The amplitude and phase measurements made by DAS are consistent with the measurements made by the geophones. The DAS data measured using both cables tends to have slightly higher amplitudes than the geophone records at near offsets.

Preprints (www.preprints.org) | NOT PEER-REVIEWED | Posted: 28 April 2022 doi:10.20944/preprints202204.0268.v1

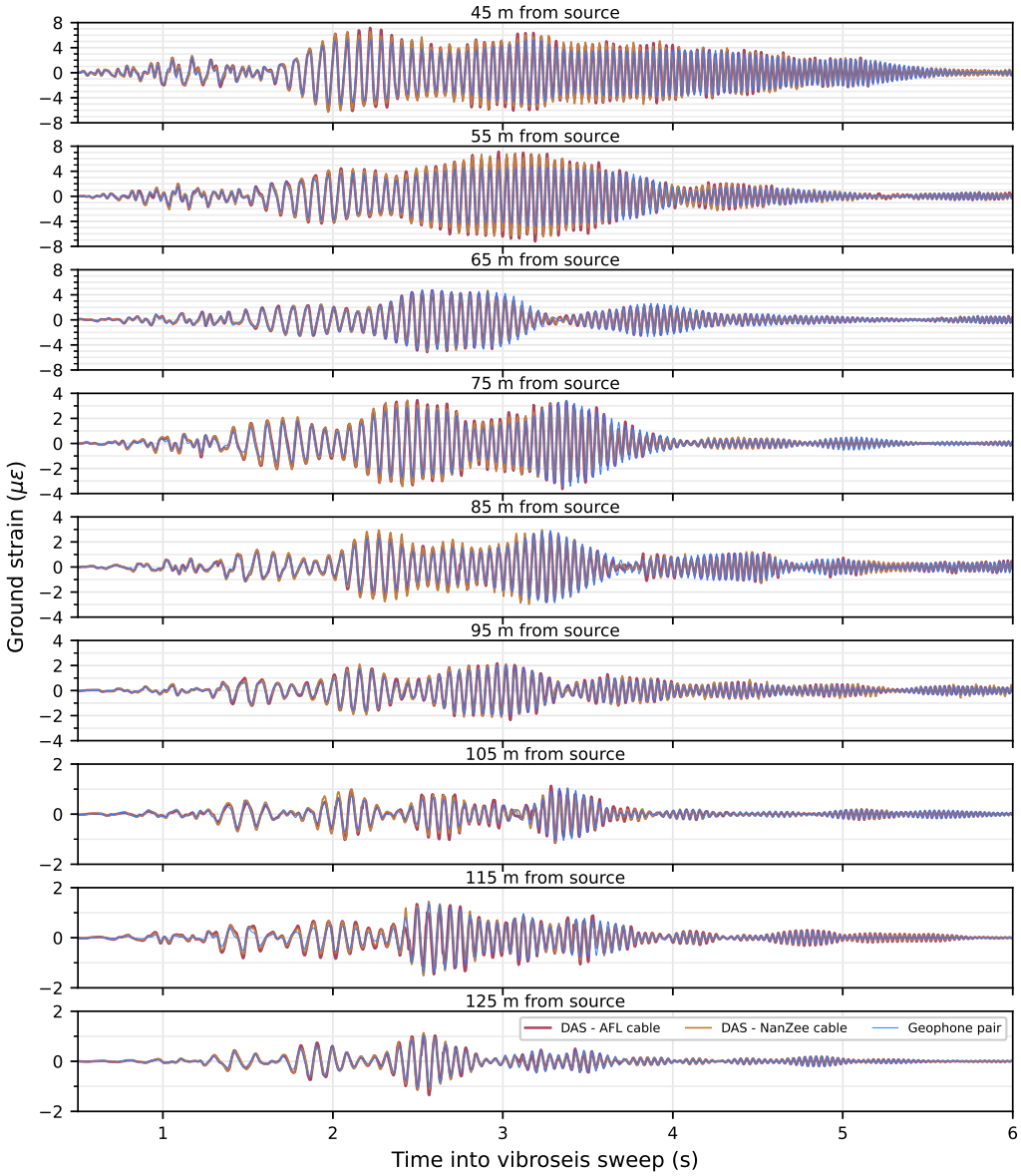

Figure 11. Spatially shifted DAS and geophone data comparisons in units of strain during 0.5-6s of vertical shaking by the T-Rex shaker truck at a position of 40 m from the array performing a 12-second, 3-80 Hz chirp. The DAS data has been spatially shifted from its positions in Figure 8 using the presented Fourier interpolation procedure to match up with the geophone data (77 cm for the NanZee cable and 30 cm for the AFL cable). The distance indicated is the point between the two spatially differenced geophones along the array.

To gain a more comprehensive picture of the comparison, the time series are visualized by their power spectra. The power spectra shown in Figure 12 are for the DAS and spatially differenced geophones centered at the same locations, as shown in Figure 11 for the frequency range of 3-100 Hz. The noise floor is also displayed for each. The noise floor was determined by taking the power spectrum of the signals during a quiet period when no shaking was happening. The DAS datasets show slightly higher signal power than the geophones across the frequency band, with the DAS showing significantly larger power above 45 Hz. The signal power difference at high frequencies has a clear cause and is discussed later.

Preprints (www.preprints.org) | NOT PEER-REVIEWED | Posted: 28 April 2022 doi:10.20944/preprints202204.0268.v1

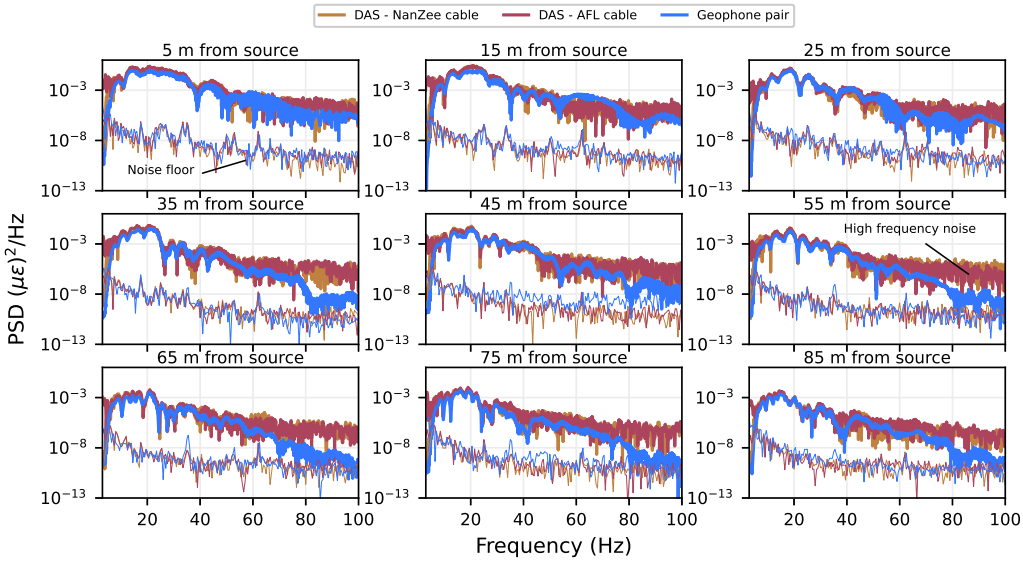

Figure 12. Power spectra of DAS and geophone data comparisons during vertical shaking by the T-Rex shaker truck at a position of 40 m from the array performing a 12-second, 3-80 Hz chirp. The noise floor for each DAS cable and the geophones has been calculated from 2 s of quiet time following the vibration.

6.4. Sledgehammer shot

The DAS and geophone-measured strain from a vertical sledgehammer striking the ground at 10 m from the arrays is presented in Figure 13. The measurements are shown for a single sledgehammer strike 0-1 s after impact. The geophone and DAS measurements agree well across the entire array from the hammer strike, indicating that DAS is a viable tool for not only measuring high amplitude vibroseis induced ground shaking but also the less energetic and more traditionally used sledgehammer.

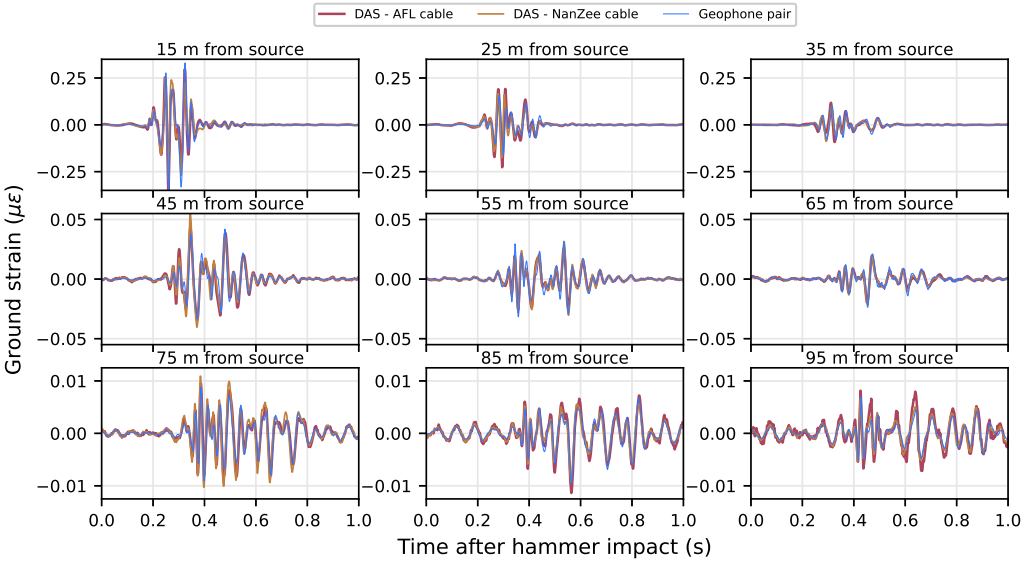

Figure 13. Spatially shifted DAS and geophone data comparisons in units of strain during a vertical sledgehammer strike 10 m from the array. The DAS data has been spatially shifted using the procedure shown in Figure 10 to align with the geophone data. The distance indicated is the point between the two spatially differenced geophones along the array.

Preprints (www.preprints.org) | NOT PEER-REVIEWED | Posted: 28 April 2022 doi:10.20944/preprints202204.0268.v1

6.5. Remarks on signal amplitude

The signals measured with DAS have a statistically larger amplitude than the geophone measurements. By examining the root-mean-square amplitude of all of the waveforms presented in this paper, the average difference in amplitude is 8.6%. The most likely cause of this mismatch is the coupling difference between the geophones and DAS. The geophones were coupled to the surface with spikes inserted into the surface soil. During installation the soil around the spike is disturbed. This may cause less of the subsurface strain to be transferred to the geophone than the DAS cable. Another possibility is the geophone calibration. A single frequency response and amplitude correction factor provided by the geophone manufacturer was used for all the geophones. This could change with use of the geophones over time and vary from one geophone to another. Each geophone should be individually calibrated for accurate quantification of amplitudes if numbers within 10% are important. Nonetheless, there is no physical reason why the DAS measurements would be too large, as the physics limits the upper bound measurements.

6.6. Remarks on noise in DAS measurements

Examining the power spectra of the DAS when recording an active source and during quiet time can be a misleading representation of the system's signal to noise ratio. There is an aspect of DAS system noise that is caused by signals that change faster than the phase can be measured, referred to here as demodulation error. This can be thought of as the DAS version of clipping when amplitudes are too large for traditional seismographs. Even though the DAS system employed a pulse rate of 100 kHz, the rate of strain change along the fiber can still exceed the maximum rate of change the DAS system can capture. The experimental results indicate that this strain rate was exceeded at times throughout the measurements. Figure 14 shows an example that occurred 2 s into the off-end vertical vibroseis sweep at a location 75 m along the DAS arrays. The DAS data from both cables shows abrupt jumps, which may be the result of demodulation errors (strain rates higher than the system's maximum). The geophone data on the other hand is smooth because it does not have this optical limitation.

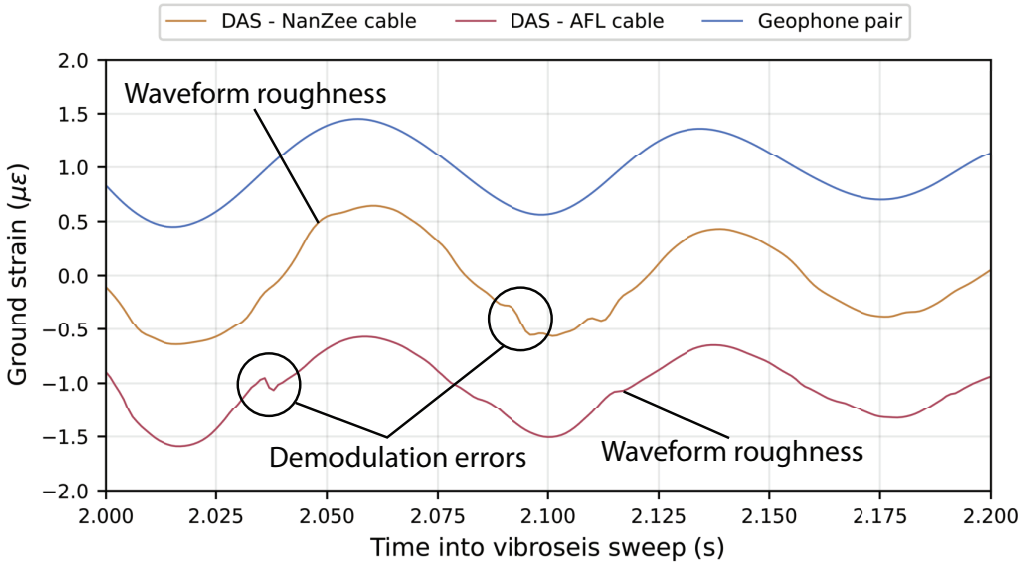

Figure 14. Close-up of the demodulation error problem that causes broadband noise in the DAS measurements at high strain-rates. The example shown is during vertical vibration when the vibroseis was located in the off-end source-receiver geometry 40m from the beginning of the arrays. The data shown in 75m along the arrays (115 m from the source). The time-series have been shifted for examination.

Preprints (www.preprints.org) | NOT PEER-REVIEWED | Posted: 28 April 2022 doi:10.20944/preprints202204.0268.v1

The abrupt jumps manifest as broadband noise in the DAS measurements only when vibration is happening. In addition to the abrupt jumps, there is general waveform roughness in the DAS data. This could be caused by imperfect coupling on the inside of the fiber optic cables, or uneven deformation of the soil surrounding the cables. Therefore, the DAS signal power appears to be higher than the geophones at frequencies above about 45 Hz in Figure 13 when it is not actually the coherent signal that is higher power. It is possible to better localize the noise in time by examining spectrograms of the records. Figure 15 shows spectrograms for both DAS cables and the geophone pair at 75 m into the arrays (115 m from the source) during the vertical vibroseis sweep. The noise that extends to high frequencies is concentrated between 2-4 seconds into the vibroseis sweep which also corresponds to the time of maximum force output by the T-Rex shaker truck. The spectrogram from the geophone measurements does not show this noise source. The 75 m location selected for Figure 15 is representative of the entire array because this noise persisted at all offsets as indicated by the high frequency power previously shown in Figure 12, though the power of the demodulation noise diminished with the power of the signal (i.e., remaining relatively constant in SNR).

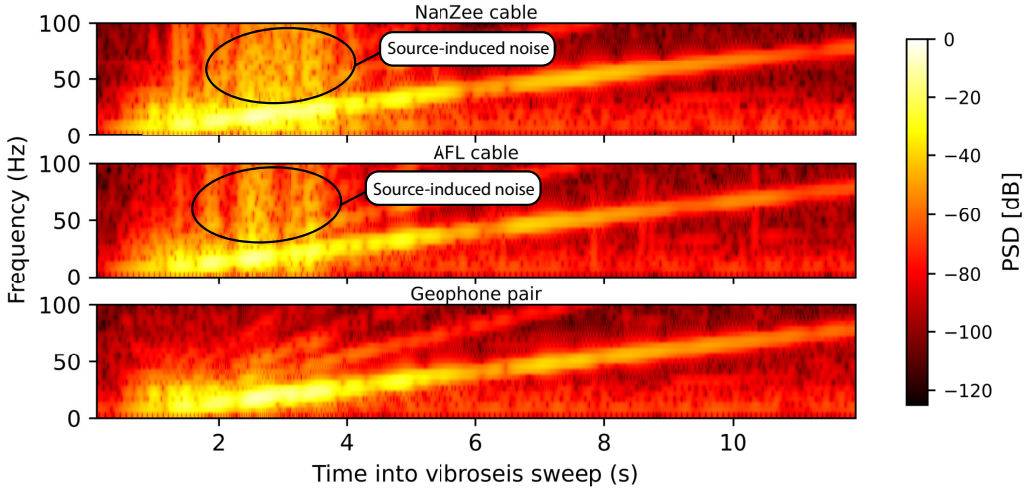

Figure 15. Spectrograms of DAS and spatially differenced geophone time-series 75m along the arrays (115 m from the source) during the vertical vibration. The spectrogram employs a 206-point FFT over a Hann window with a 205-point overlap between windows. All signals were processed at 1000 Hz sampling rate.

7. Conclusions

The potential for using DAS as an engineering tool for applications such as FWI imaging, dynamic ground deformation measurements and soil-structure interaction studies relies on understanding the both the amplitude and phase measurements made by DAS. DAS deployment, quantification, channel positioning, and numerical simulation techniques in this study aim to demonstrate DAS as a viable sensing tool for these types of uses.

A gauge length versus wavelength relationship was derived for various source-to-array geometries by examining the theoretical reception patterns and using 3D finite-difference simulations of wave propagation in an elastic solid. This was done for active sources with vertical and horizontal polarizations. It was found that the wavelength versus gauge length relationship is critical for fully capturing pointwise strain waveforms, and this relationship must be understood for effective quantitative deployments where pointwise strain is desired. However, it was demonstrated that strain measured with DAS is easily modeled as a difference of the displacement field over the system's gauge length, allowing for forward-modeled problems to solve for the DAS measurand directly.

Once the theoretical DAS response to ground deformation was developed, an experimental comparison of measurements made by geophones and DAS using a large vibroseis truck and sledgehammer strike was presented. It is shown that DAS measures ground deformation quantitatively with both amplitude and phase that agree with measurements made by geophones. The reception characteristics are consistent with the theory and simulation results including predictable zones of zero reception and changes in the sign (phase-flips) of the measured strain.

This study demonstrates that certain key steps need to be undertaken to ensure the quality of the DAS measurements and their comparison to geophones. Those key steps are: (1) aligning the DAS channels and geophones using a new method presented in this paper, (2) selecting a DAS cable that provides deformation coupling to the internal optical fiber, (3) coupling the cable to the ground through direct burial and compaction, and (4) laser phase noise mitigation through high pass filtering the DAS measurements. After these steps were taken, the DAS measurements and geophone measurements were shown to be very consistent with each other in both phase and amplitude. This method was demonstrated using two different suitable cables for direct buried DAS arrays. A source of broadband noise, demodulation error, is discussed for its impact on the signal spectra of DAS measurements, but is shown to have limited impacts on the waveform comparisons between DAS and geophones.

Author Contributions: Conceptualization, P.H., B.C., K.S., and J.R.; methodology, B.C and P.H.; software, J.V.; validation, P.H. and J.V.; formal analysis, P.H. and J.V.; investigation, B.C., J.V., M.Y., and P.H.; resources, B.C. and K.S.; data curation, M.Y. and J.V.; writing—original draft preparation, P.H.; writing—review and editing, P.H., J.V., B.C, J.R., M.Y., and K.S.; visualization, P.H. and J.V.; supervision, B.C. and K.S.; project administration, B.C.; funding acquisition, B.C. and K.S. All authors have read and agreed to the published version of the manuscript.

Funding: This work was supported in part by the U.S. National Science Foundation (NSF) grants CMMI-2037900, CMMI-1520808, and CMMI-1931162. However, any opinions, findings, and conclusions or recommendations expressed in this material are those of the authors and do not necessarily reflect the views of NSF.

Data Availability Statement: The data presented in this study are openly available in DesignSafe-CI at [DOI: 10.17603/ds2-bz52-ep82], reference number [28].

Acknowledgments: Special thanks to Dr. Kevin Anderson at Austin Water – Center for Environmental Research for the access to the Hornsby Bend Biosolids Management Plant test site. Special thanks to Todd Bown, Martin Karrenbach and the Optasense team for their assistance in configuring the ODH4 and providing information about its operation. The Optasense team also helped with extracting and post-processing the seismic waveforms, and permitting us to publish these results. The figures in this paper were created using Matplotlib 3.1.2 [29].

Conflicts of Interest: The authors declare no conflict of interest.

References

1. Hartog, A. *An Introduction to Distributed Optical Fibre Sensors*; CRC Press, 2018.
2. Nakazawa, M. Rayleigh backscattering theory for single-mode optical fibers. *JOSA* **1983**, *73*, 1175–1180. doi:10.1364/JOSA.73.001175.
3. Giallorenzi, T.G.; Sigel, G.H.; Bucaro, J.A. Optical fiber sensor technology. *Optica Publishing Group* **1982**, p. ThGG1. doi:10.1364/OFC.1982.ThGG1.
4. Ogden, H.M.; Murray, M.J.; Murray, J.B.; Kirkendall, C.; Redding, B. Frequency multiplexed coherent φ-OTDR. *Sci. Rep.* **2021**, *11*, 1–12. doi:10.1038/s41598-021-97647-z.
5. Daley, T.M.; Freifeld, B.M.; Ajo-Franklin, J.; Dou, S.; Pevzner, R.; Shulakova, V.; Kashikar, S.; Miller, D.E.; Goetz, J.; Henninges, J.; et al. Field testing of fiber-optic distributed acoustic sensing (DAS) for subsurface seismic monitoring. *Leading Edge* **2013**, *32*, 699–706. doi:10.1190/tle32060699.1.
6. Titov, A.; Binder, G.; Liu, Y.; Jin, G.; Simmons, J.; Tura, A.; Monk, D.; Byerley, G.; Yates, M. Modeling and interpretation of scattered waves in interstage distributed acoustic sensing vertical seismic profiling surveyScattered waves in interstage DAS VSP. *Geophysics* **2021**, *86*, D93–D102. doi:10.1190/geo2020-0293.1.

7. Dou, S.; Lindsey, N.; Wagner, A.M.; Daley, T.M.; Freifeld, B.; Robertson, M.; Peterson, J.; Ulrich, C.; Martin, E.R.; Ajo-Franklin, J.B. Distributed Acoustic Sensing for Seismic Monitoring of The Near Surface: A Traffic-Noise Interferometry Case Study. *Sci. Rep.* **2017**, *7*, 1–12. doi:10.1038/s41598-017-11986-4.
8. Ajo-Franklin, J.B.; Dou, S.; Lindsey, N.J.; Monga, I.; Tracy, C.; Robertson, M.; Rodriguez Tribaldos, V.; Ulrich, C.; Freifeld, B.; Daley, T.; et al. Distributed Acoustic Sensing Using Dark Fiber for Near-Surface Characterization and Broadband Seismic Event Detection. *Sci. Rep.* **2019**, *9*, 1–14. doi:10.1038/s41598-018-36675-8.
9. Lindsey, N.J.; Dawe, T.C.; Ajo-Franklin, J.B. Illuminating seafloor faults and ocean dynamics with dark fiber distributed acoustic sensing. *Science* **2019**, *366*, 1103–1107. doi:10.1126/science.aay5881.
10. Williams, E.F.; Fernández-Ruiz, M.R.; Magalhaes, R.; Vanthillo, R.; Zhan, Z.; González-Herráez, M.; Martins, H.F. Distributed sensing of microseisms and teleseisms with submarine dark fibers. *Nat. Commun.* **2019**, *10*, 1–11. doi:10.1038/s41467-019-13262-7.
11. Daley, T.M.; Miller, D.E.; Dodds, K.; Cook, P.; Freifeld, B.M. Field testing of modular borehole monitoring with simultaneous distributed acoustic sensing and geophone vertical seismic profiles at Citronelle, Alabama. *Geophys. Prospect.* **2016**, *64*, 1318–1334. doi:10.1111/1365-2478.12324.
12. Dean, T.; Cuny, T.; Hartog, A.H. The effect of gauge length on axially incident P-waves measured using fibre optic distributed vibration sensing. *Geophys. Prospect.* **2017**, *65*, 184–193. doi:10.1111/1365-2478.12419.
13. Wang, H.F.; Zeng, X.; Miller, D.E.; Fratta, D.; Feigl, K.L.; Thurber, C.H.; Mellors, R.J. Ground motion response to an ML 4.3 earthquake using co-located distributed acoustic sensing and seismometer arrays. *Geophys. J. Int.* **2018**, *213*, 2020–2036. doi:10.1093/gji/ggy102.
14. Mateeva, A.; Lopez, J.; Potters, H.; Mestayer, J.; Cox, B.; Kiyashchenko, D.; Wills, P.; Grandi, S.; Hornman, K.; Kuvshinov, B.; et al. Distributed acoustic sensing for reservoir monitoring with vertical seismic profiling. *Geophys. Prospect.* **2014**, *62*, 679–692. doi:10.1111/1365-2478.12116.
15. Song, Z.; Zeng, X.; Thurber, C.H. Surface-wave dispersion spectrum inversion method applied to Love and Rayleigh waves recorded by distributed acoustic sensing. *Geophysics* **2021**. doi:10.1190/geo2019-0691.1.
16. Vantassel, J.P.; Cox, B.R.; Hubbard, P.G.; Yust, M. Extracting High-Resolution, Multi-Mode Surface Wave Dispersion Data from Distributed Acoustic Sensing Measurements using the Multichannel Analysis of Surface Waves. *arXiv* **2022**. doi:10.48550/arXiv.2202.04779.
17. Virieux, J.; Operto, S. An overview of full-waveform inversion in exploration geophysics. *Geophysics* **2009**, *74*, WCC1–WCC26. doi:10.1190/1.3238367.
18. Egorov, A.; Correa, J.; Bóna, A.; Pevzner, R.; Tertyshnikov, K.; Glubokovskikh, S.; Puzyrev, V.; Gurevich, B. Elastic full-waveform inversion of vertical seismic profile data acquired with distributed acoustic sensors. *Geophysics* **2018**. doi:10.1190/geo2017-0718.1.
19. Eaid, M.V.; Keating, S.D.; Innanen, K.A. Multiparameter seismic elastic full-waveform inversion with combined geophone and shaped fiber-optic cable dataFWI with combined geophone and DAS data. *Geophysics* **2020**, *85*, R537–R552. doi:10.1190/geo2020-0170.1.
20. Masoudi, A.; Newson, T.P. Contributed Review: Distributed optical fibre dynamic strain sensing. *Rev. Sci. Instrum.* **2016**, *87*, 011501. doi:10.1063/1.4939482.
21. Benioff, H. A linear strain seismograph. *Bull. Seismol. Soc. Am.* **1935**, *25*, 283–309. doi:10.1785/BSSA0250040283.
22. Martin, E.R.; Lindsey, N.J.; Ajo-Franklin, J.B.; Biondi, B.L. Introduction to Interferometry of Fiber-Optic Strain Measurements. In *Distributed Acoustic Sensing in Geophysics*; American Geophysical Union (AGU), 2021; pp. 111–129. doi:10.1002/9781119521808.ch9.
23. Petersson, N.A.; Sjogreen, B. geodynamics/sw4: SW4, version 2.0. *Zenodo* **2017**. doi:10.5281/zenodo.1045297.
24. Achenbach, J.D. *Wave Propagation in Elastic Solids*; Elsevier: Amsterdam, 1999.
25. Stokoe, K.H.I.I.; Cox, B.R.; Clayton, P.M.; Menq, F. NHERI@UTexas Experimental Facility With Large-Scale Mobile Shakers for Field Studies. *Front. Built Environ.* **2020**, *0*. doi:10.3389/fbuil.2020.575973.
26. Weik, M.H. *Fiber Optics Standard Dictionary*; Chapman and Hall, 1997.
27. Oppenheim, A.V.; Buck, J.R.; Schafer, R.W. *Discrete-time Signal Processing (2nd Ed.)*; Prentice Hall, 1999.
28. Vantassel, J.P.; Cox, B.R.; Hubbard, P.G.; Yust, M.; Menq, F. Characterization of the NHERI@UTexas Hornsby Bend Test Site. *DesignSafe-CI* **2022**. doi:10.17603/ds2-bz52-ep82.
29. Hunter, J.D. Matplotlib: A 2D Graphics Environment. *Comput. Sci. Eng.* **2007**, *9*, 90–95. doi:10.1109/MCSE.2007.55.